Supplementary material for:

Ambient noise Rayleigh wave tomography across the Madagascar island.

Adimah Nicholas Irabor[*,a,b] **and Simanchal Padhy**[a,b]

[a]National Geophysical Research Institute (Council of Scientific and Industrial Research), Uppal Road, Hyderabad-500007, India

[b]Academy of Scientific and Innovative Research (AcSIR), Ghaziabad- 201002, India.

[*]Corresponding author: Adimah Nicholas Irabor

Email: adimah.nick@ngri.res.in, nickydof@yahoo.com

1. Dispersion curves in different geological settings

Here, we show the nature of dispersion curves in different geological settings like sedimentary formations and Precambrian basements. Supplementary Fig. S1(a) shows the Rayleigh wave group velocity dispersion curves for station pairs: ANTS-DGOS, BANJ-DGOS, BANJ-BERG, BERG-DGOS, CPSM-KIRI and CPSM-LONA located in the sedimentary formations of Madagascar (Fig. 1 in main text).

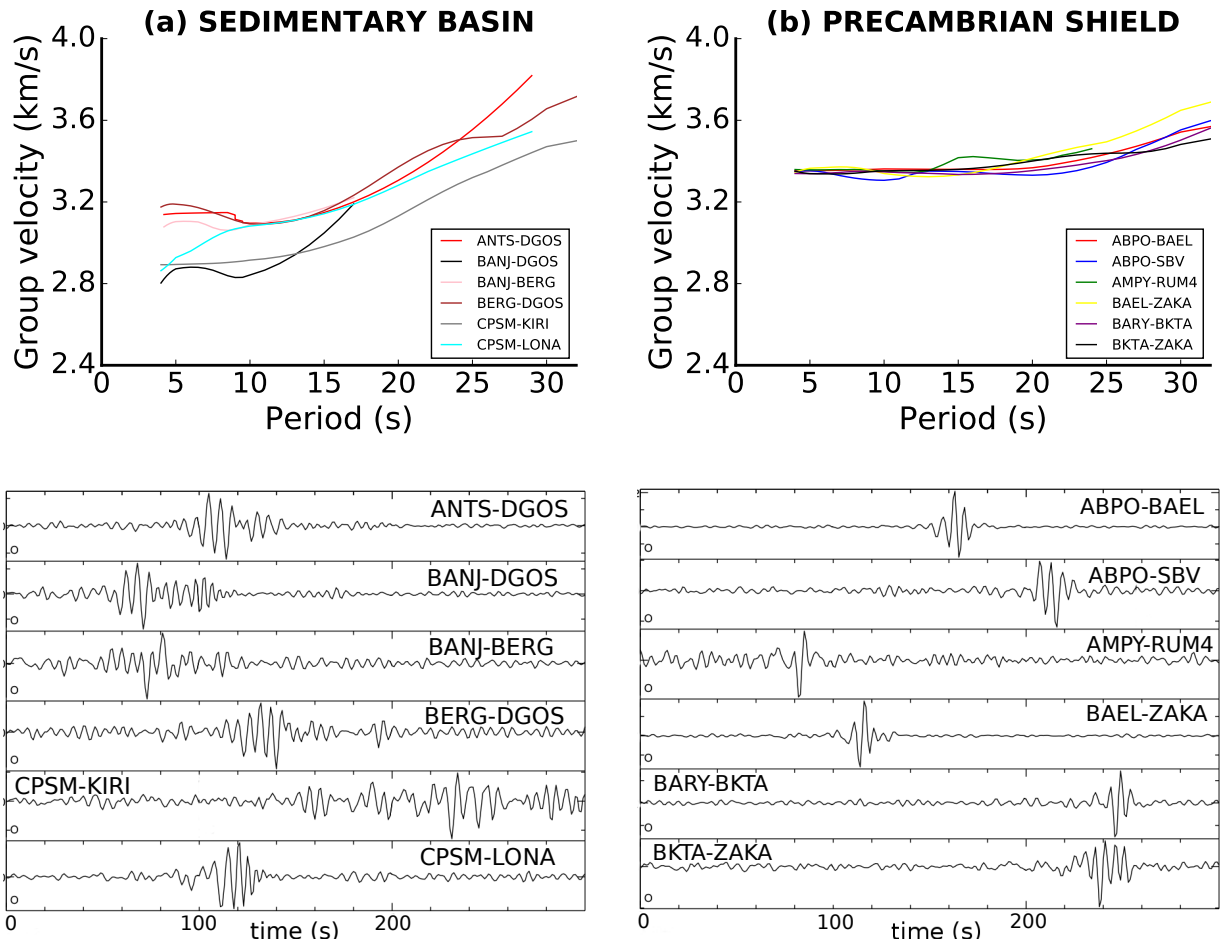

Fig. S1: (a) The upper panel shows Rayleigh wave group velocity dispersion curves measured for station pairs in the sedimentary basin while the lower panel shows their corresponding cross-correlation waveforms. (b) same as in (a) but for stations in the Precambrian shield.

These curves show low velocities at short periods, suggesting the presence of thick sediments. Increasing sensitivity to the basement material with increasing wave speed is responsible for their relatively large slope. On the other hand, Fig S1(b) shows similar curves as in Fig. S1(a) but for station pairs: ABPO-BAEL, ABPO-SBV, AMPY-RUM4, BAEL-ZAKA, BARY-BKTA and BKTA-ZAKA deployed in the Precambrian basement. These curves are distinctly different from those in the sedimentary basins, showing relatively high velocities over the entire period

range, indicating the presence of thick crust along the propagation path. Corresponding station pair cross-correlation waveforms are shown in the bottom panels of Fig. S1(a) and (b).

2. Selection of inversion parameters for tomography

The tomographic inversion was performed following the method due to Barmin *et al.*, 2001. As already decribed in the main text, the inversion invloves a careful selection of these four parameters: $\alpha, \beta, \sigma, \lambda$. The inversion is performed in two steps. In the first step, we assign a large strength to the spatial smoothing condition ($\alpha = 3000$), generating overly smoothed maps at each period in order to identify and reject bad measurements.

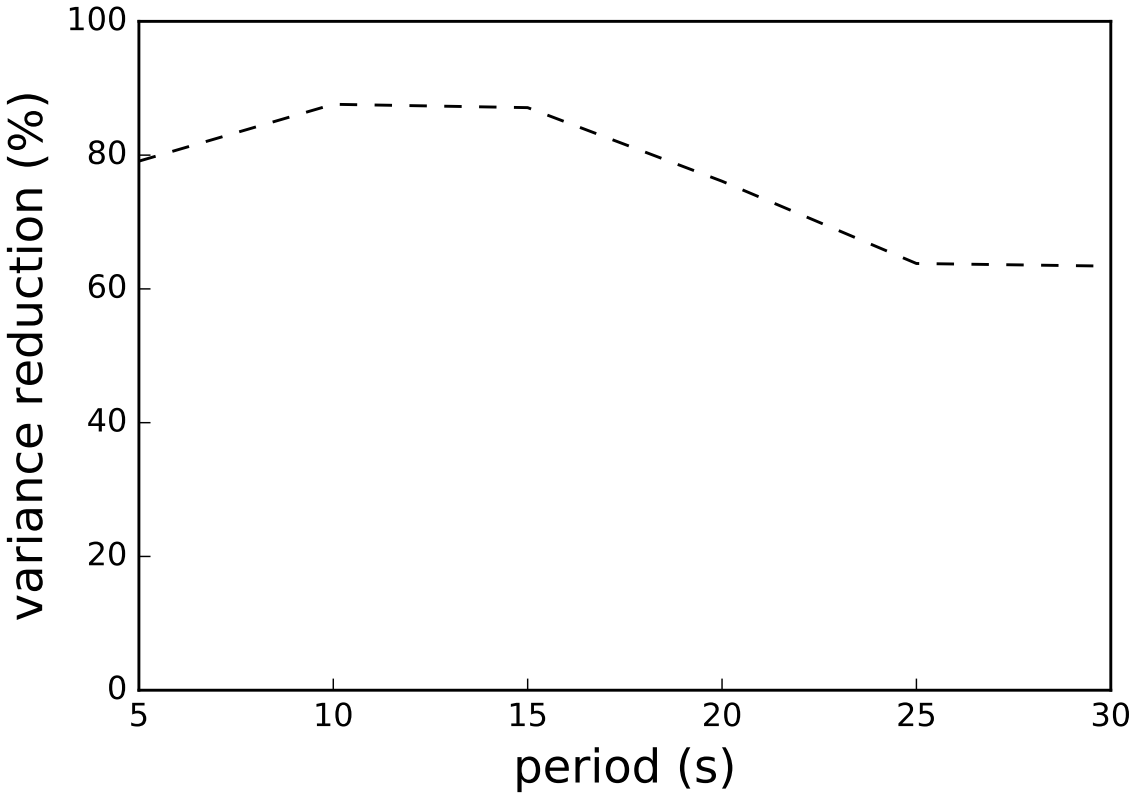

Fig. S2: Misfit is presented as reduction of variance delivered by the estimated maps relative to the predicted group velocity maps.

Data for station pairs whose travel time residual is larger than trice the standard deviation of the residuals are discarded and then the second step inversion is carried out to construct the final maps. Because the choice of the damping parameters α and β and the smoothing width σ is subjective, in this step, we perform a number of tests using different combinations of these parameters to determine optimal values by considering data misfit, model resolution, model

norm and stability of the features in the resulting models. The optimal values are shown in Table 1 in the main text. As can be seen in Fig. S2, the success of the final models (generated using the optimal inversion parameters) in fitting the data is quite good. With exception of the 30 s period, variance reduction exceeds 70 % for all periods, signifying improvement in fit to the measured dispersion curves achieved by the resulting group velocity maps.

3. Resolution analysis

We have investigated the resolving power of our tomographic maps using three schemes: path coverage, spatial resolution (Barmin *et al.*, 2001) and the well-known "checkerboard" resolution test (Fig. 8 in main text). For the checkerboad test, anomaly size of ~ 250 km which was well recovered across all periods was used (right panel of Fig. 8 and Fig. S3 here). However, the spatial resolution test (middle panel of Fig. 8) reveals that resolution is upto 150 km at the centers of the short period tomographic maps. To corroborate this, we further investigated the resolution of our results using the checkerboard test with smaller sized checkerboard patterns. We constructed testing models with smaller checker sizes (e.g., 120, 150, 160, 170, 180, 190 and 200 km) with ± 10 % velocity perturbations. Gaussian noise was added to mimic the error in data. Synthetic travel time data were then generated for the same distributions of observed interstation paths. Using the same inversion scheme, the synthetic data were inverted for the group velocity maps and the recovered images were compared with the original testing models (left panel in Fig. S4). The test results show that for the 5 and 10 s periods, resolution is upto 150 km while for the 20 s period map, structures with sizes ~ 200 km are resolvable (Fig. S4).

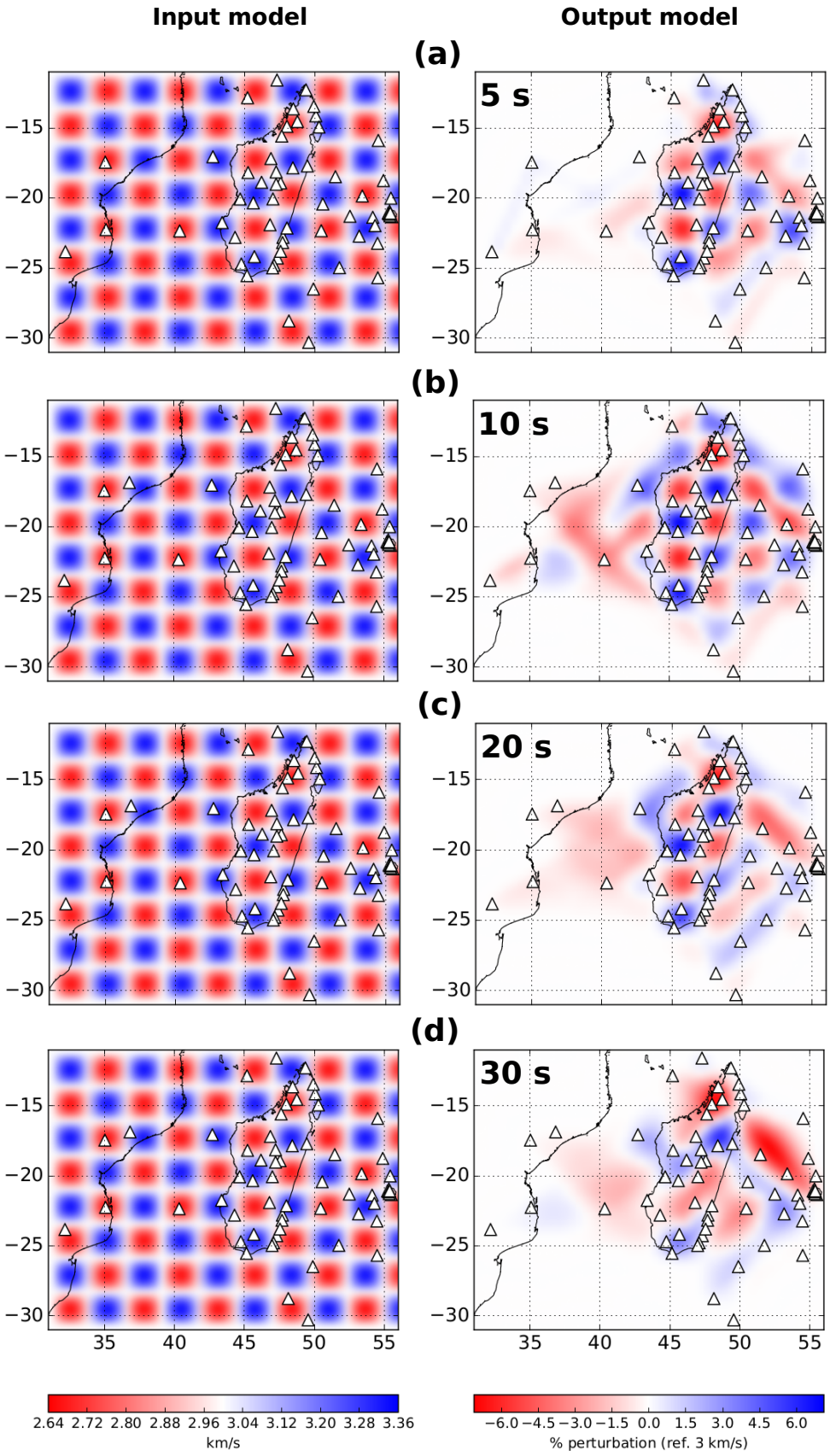

Fig. S3: 2.5^o (~ 250 km) anomaly size checkerboard test for 5, 10, 20 and 30 s periods.

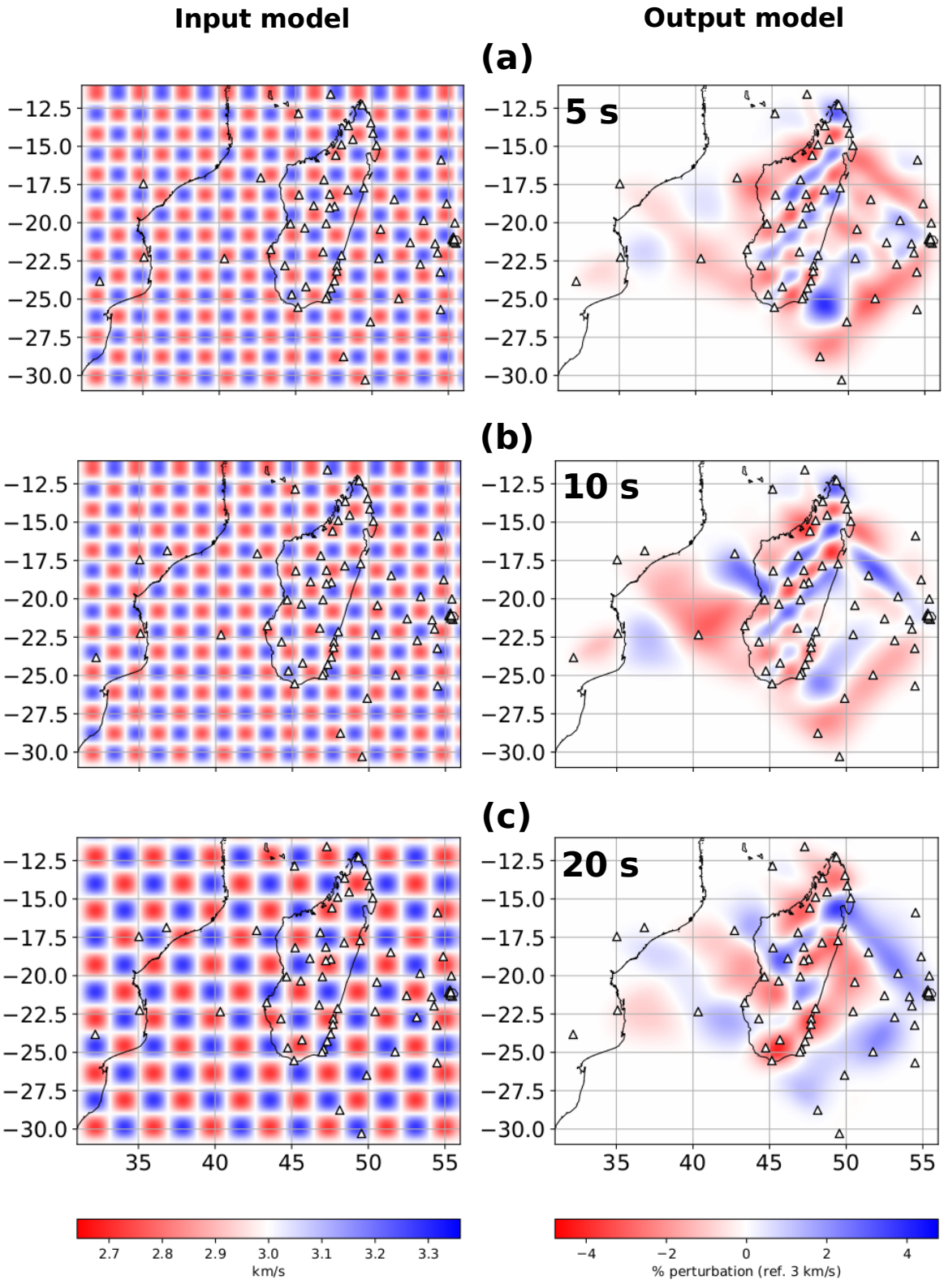

Fig. S4: 150 km anomaly size checkerboard test for 5 and 10 s periods. 200 km anomaly size test for 20 s period.

4. 3-D Vs maps at 30 and 40 km depths

As mentioned in the main text, our shear wave velocity inversion results show relative inconsistency at depths beyond 23 km when different starting models are used. This implies that our result beyond the 23 km depth is relatively not reliable. In general, Rayleigh wave group velocity dispersion data at 20 - 30 s are sensitive to shear wave velocities at depths up to around 30 - 50 km, but our poorly resolved group velocity map at the 30 s period is most likely responsible for our inability to constrain the Vs structure up to these deeper depths. To this end, we have only shown shear wave velocity slices at depths within 0 - 23 km in the main text. Shear velocity maps at depths beyond 23 km, e.g., 30 and 40 km (Fig. S5) appear heavily smoothened even though they show some resemblance with the major geological features in the lower crust and uppermost mantle beneath the study area.

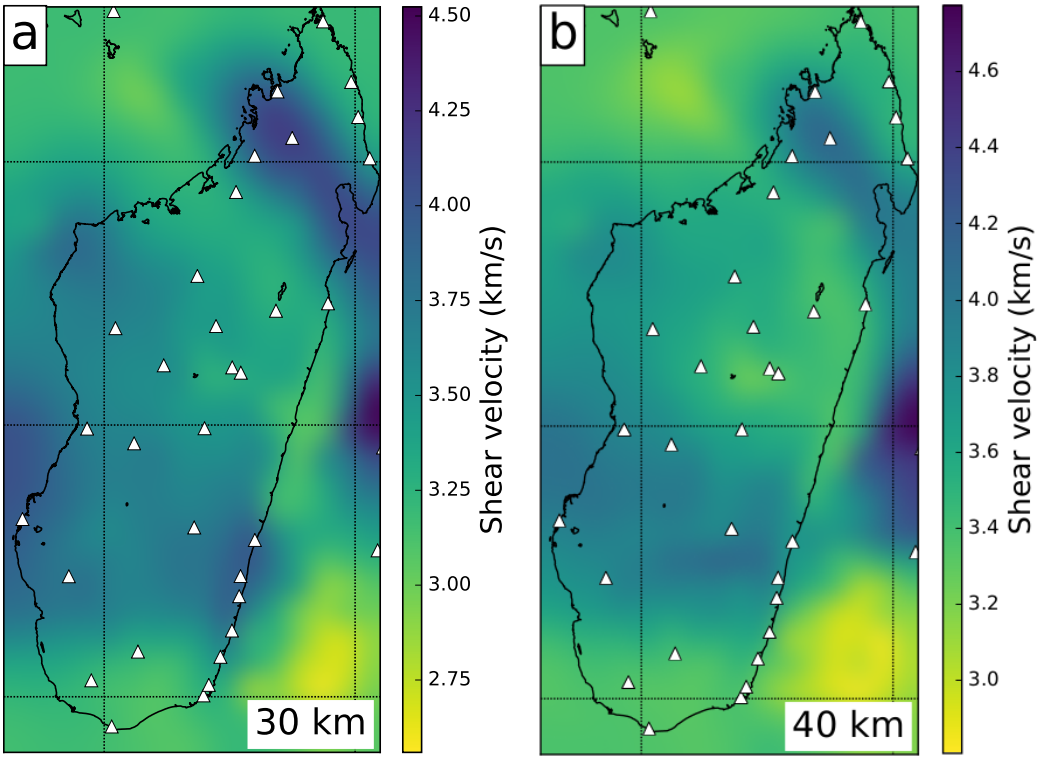

Fig. S5: 3-D Vs models at 30 and 40 km depths.

Table S1: Seismic broad-band stations used in this study.

Station ID	**Network**	**Latitude(^{o})**	**Longitude(^{o})**	**Station ID**	**Network**	**Latitude(^{o})**	**Longitude(^{o})**
AMPY	XV	-24.7033	44.7435	ETAN	YV	-21.2672	55.3526
ANLA	XV	-17.7062	49.4599	EURO	YV	-22.3440	40.3401
ANTS	XV	-14.8843	47.9992	GLOR	YV	-11.5824	47.2895
BAEL	XV	-14.5397	48.7476	JNOV	YV	-17.0543	42.7125
BAND	XV	-20.3428	45.5964	MAID	YV	-21.0797	55.3831
BANJ	XV	-13.6426	48.4537	MAYO	YV	-12.8456	45.1868
BARY	XV	-17.1845	46.8571	POSS	YV	-20.9363	55.3263
BATG	XV	-18.8785	46.1870	RR01	YV	-20.0069	55.4230
BERG	XV	-15.5800	47.6277	RR03	YV	-21.3732	54.1294
BITY	XV	-20.0608	47.0000	RR18	YV	-18.7504	54.8878
BKTA	XV	-24.1821	45.6730	RR19	YV	-19.8500	53.3805
CPSM	XV	-25.5358	45.1500	RR20	YV	-18.4774	51.4600
DGOS	XV	-12.2825	49.3606	RR21	YV	-20.4217	50.5599
KIRI	XV	-20.0676	44.6595	RR22	YV	-21.3007	52.4994
LAHA	XV	-14.9344	50.2911	RR23	YV	-22.3290	50.4487
LONA	XV	-22.8057	44.2958	RR24	YV	-25.6805	54.4881
MAHA	XV	-23.1714	47.6898	RR25	YV	-23.2662	56.7249
MAPH	XV	-22.2500	35.0800	RR26	YV	-23.2293	54.4698
MKVA	XV	-14.1368	50.0607	RR27	YV	-21.9657	54.2889
MMBE	XV	-21.7500	43.3721	RR28	YV	-22.7152	53.1594
MOCU	XV	-16.8600	36.8300	RR29	YV	-24.9657	51.7488
MSGR	XV	-23.8300	32.1800	RR30	YV	-26.4861	49.8917
SENA	XV	-17.4450	35.0320	RR31	YV	-28.7648	48.1394
TANS	XV	-18.9176	47.5511	RR32	YV	-30.2903	49.5555
VINA	XV	-18.1769	45.2247	RUM1	YV	-22.8022	47.7175
ZAKA	XV	-17.8470	48.4230	RUM2	YV	-22.1367	48.0022
ZOBE	XV	-18.1369	47.2289	RUM3	YV	-23.7988	47.5459
ABPO	II	-19.0180	47.2290	RUM4	YV	-24.2767	47.3157
FOMA	G	-24.9756	46.9788	RUM5	YV	-24.7852	47.0851
SBV	GE	-13.4584	49.9212	SGIL	YV	-21.0774	55.7644
VOI	GE	-21.9064	46.7932	TROM	YV	-15.8885	54.5218
CBNM	YV	-21.1381	55.2960				

5. Tilt and compliance noise reduction

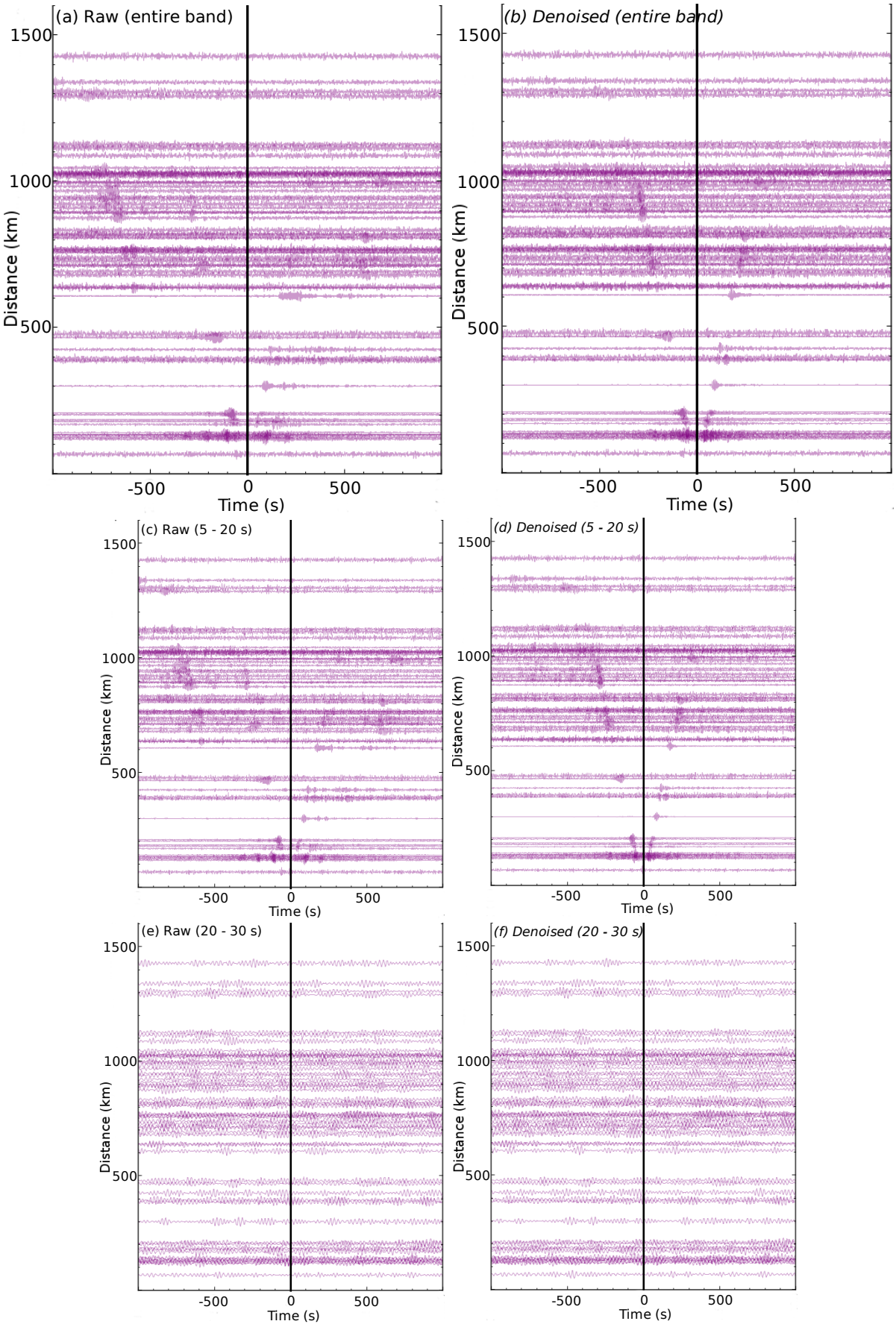

Fig. S6: Record sections of vertical component CCFs for OBS station RR03. (a) Unfiltered Raw CCFs computed without correcting for tilt and compliance noise. (b) Similar to (a), but tilt and compliance noise removed. (c) Similar to (a), but filtered between 5 - 20 s period. (d) Similar to (c), but filtered between 5 - 20 s period. (e) Similar to (a), but filtered between 20 - 30 s period. (f) Similar to (c), but filtered between 20 - 30 s period.

To assess the effectiveness of the denoising procedure on the ambient noise CCFs, we compute the CCFs before (raw CCFs) and after (denoised CCFs) applying the denoising procedure. Record sections of the OBS station RR03 are plotted in Fig. S6 for both raw and denoised CCFs. In the unfiltered (Fig. S6a), 5 - 20 s period band (Fig. S6c) and 20 - 30 s period band (Fig. S6e), the observed signal on the raw CCFs are weak. On the other hand, in the unfiltered (Fig. S6b) and 5 - 20 s period band (Fig. S6d) denoised CCFs, the signal is moderately improved. Unfortunately, in the 20 - 30 s period band (Fig. S6f) of the denoised CCFs, the signal is still weak. These observations are consistent with the SNR results shown in Fig. 5 in the main text where the denoising procedure shows to have more effect at the short to middle periods (5 - 20 s) compared with the long periods (> 20 s).

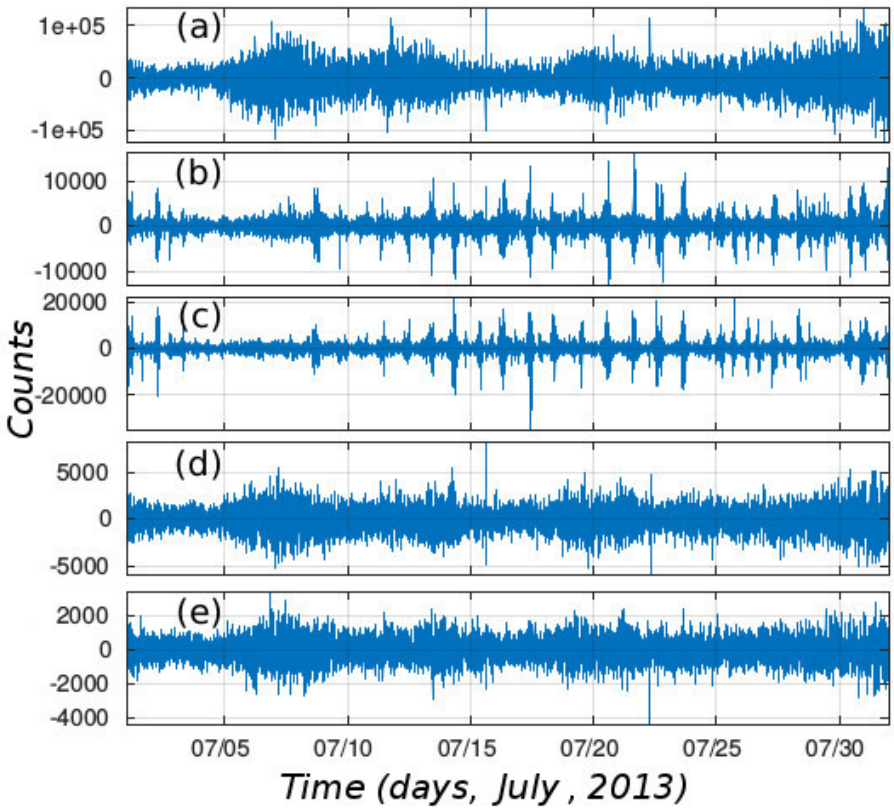

Fig. S7: A plot of approximately one month (July, 2013) long raw and corrected signals from the OBS station RR03 of the RHUM-RUM network. From (a) to (e): raw pressure record, raw N-S component, raw E-W component, raw Z component and Z component after removing coherent pressure and horizontal signals. Note, a moderately strong coherence between the pressure and vertical component records shown in (a) and (d), respectively..

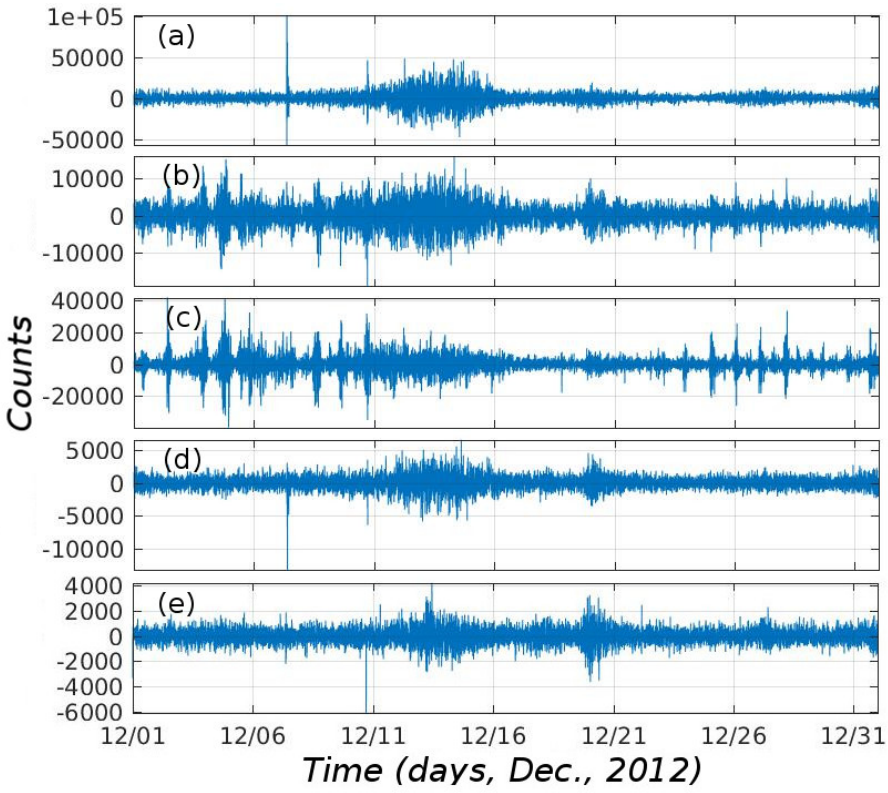

Fig. S8: Same as in Fig. S7 but for OBS station RR21.

We can also assess the effectiveness of the denoising procedure directly from the raw and denoised waveform data. In Fig. S7, there is a moderately strong coherence between the pressure record (Fig. S7a) and the raw vertical record (Fig. S7d) of OBS station RR03 between the 11^{th} and 16^{th} day, signifying strong contamination by compliance noise. However, comparing the denoised vertical waveform (Fig. S7e) with the pressure record (Fig. S7a), the earlier seen coherence is almost completely removed. This shows that the denoising procedure was fairly effective in suppressing the contaminant noises. A similar reduction in compliance and tilt noise is also seen in Fig. S8 for OBS station RR21.

6. SNR calculation

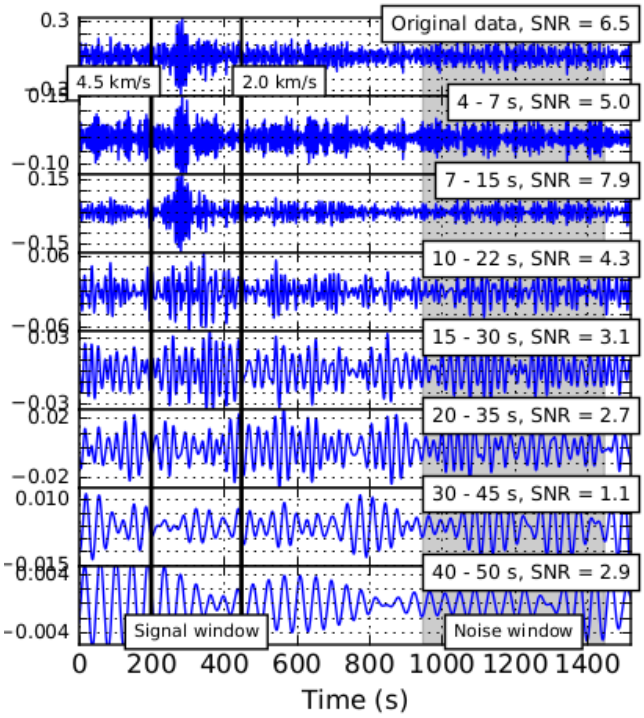

Fig. S9: Calculation of SNR shown for CCF between stations BARY and RR03. SNR is the ratio of the maximum absolute amplitude in the signal window to the standard deviation in the noise window. The signal is the window that spans arrival times corresponding to velocities between 2 and 4.5 km/s (thick vertical black lines) while the noise window has a width of 500 s and starts 500 s after the signal window (grey patch).